

Article

Manganese-Based Metal-Organic Frameworks Photocatalysts for Visible Light-Driven Oxidative Coupling of Benzylamine under Atmospheric Oxygen: A Comparative Study

Lamia A. Siddig, Reem H. Alzard , Abdalla S. Abdelhamid and Ahmed Alzamly * 

Department of Chemistry, United Arab Emirates University, Al-Ain P.O. Box 15551, United Arab Emirates

* Correspondence: ahmed.alzamly@uaeu.ac.ae

Abstract: Research on the utilization of sustainable and renewable energy sources has increased as a result of the world's expanding energy demand. In this regard, we report the photocatalytic performance of two synthesized Mn-MOFs: $\text{Mn}^{\text{II}}_3(\text{tp})_{6/2}(\text{bpy})_2 \cdot (\text{dmf})$ ($\text{C}_{47}\text{H}_{35}\text{Mn}_3\text{N}_5\text{O}_{13}$) and $\text{Mn}_2(\text{tpa})_2(\text{dmf})_2$ ($\text{C}_{22}\text{H}_{22}\text{Mn}_2\text{N}_2\text{O}_{10}$). The two MOFs were characterized using different spectroscopic and analytical techniques: powder X-ray diffraction, thermogravimetric analysis, diffuse reflectance spectroscopy, Fourier transform infrared spectroscopy, energy-dispersive X-ray spectroscopy, and scanning electron microscopy. $\text{Mn}^{\text{II}}_3(\text{tp})_{6/2}(\text{bpy})_2 \cdot (\text{dmf})$ possesses a band gap value of 2.5 eV, which exhibits significant photocatalytic activity when exposed to simulated visible light irradiation. $\text{Mn}_2(\text{tpa})_2(\text{dmf})_2$ shows a larger band gap of 3.16 eV, which renders the photocatalytic performance under visible light. The oxidation of benzylamine to *N,N*-benzylidenebenzylamine by a photocatalytic reaction was selected to evaluate the photocatalytic activities of $\text{Mn}^{\text{II}}_3(\text{tp})_{6/2}(\text{bpy})_2 \cdot (\text{dmf})$ and $\text{Mn}_2(\text{tpa})_2(\text{dmf})_2$ in the visible region. In addition to its high photocatalytic performance, $\text{Mn}^{\text{II}}_3(\text{tp})_{6/2}(\text{bpy})_2 \cdot (\text{dmf})$ also showed high thermal stability up to 430 °C. Accordingly, the strategy of designing frameworks possessing mixed ligands provides stability to the frameworks as well as enhancing the photocatalytic performance of frameworks containing bipyridine ligands such as $\text{Mn}^{\text{II}}_3(\text{tp})_{6/2}(\text{bpy})_2 \cdot (\text{dmf})$.

Keywords: $\text{Mn}^{\text{II}}_3(\text{tp})_{6/2}(\text{bpy})_2 \cdot (\text{dmf})$; $\text{Mn}_2(\text{tpa})_2(\text{dmf})_2$; band gap; metal-organic framework; visible light; photocatalyst



Citation: Siddig, L.A.; Alzard, R.H.; Abdelhamid, A.S.; Alzamly, A. Manganese-Based Metal-Organic Frameworks Photocatalysts for Visible Light-Driven Oxidative Coupling of Benzylamine under Atmospheric Oxygen: A Comparative Study. *Catalysts* **2023**, *13*, 613. <https://doi.org/10.3390/catal13030613>

Academic Editor: Carolina Belver

Received: 28 February 2023

Revised: 15 March 2023

Accepted: 16 March 2023

Published: 18 March 2023



Copyright: © 2023 by the authors. Licensee MDPI, Basel, Switzerland. This article is an open access article distributed under the terms and conditions of the Creative Commons Attribution (CC BY) license (<https://creativecommons.org/licenses/by/4.0/>).

1. Introduction

In recent years, environmental pollution and energy shortages have received tremendous attention [1]. In this regard, solar-driven technologies have been intensively studied as an alternative to overcome these problems. Moreover, using solar energy to drive chemical transformations on semiconductor photocatalysts is a viable technology for meeting clean and sustainable energy demands [2–4]. In the past few decades, numerous methods have been created to address the significant limitations of semiconductor photocatalysts, including low recyclability, limited visible-light absorption, fast charge recombination, and low quantum efficiency [1]. As a result, different approaches have been implemented in an effort to address these issues, including heterojunction creation [5,6], doping another semiconductor photocatalyst [5,7], and composite fabrication [8,9]. Visible light from total incident solar irradiation accounts for nearly 45%, making the use of visible light more viable for future practical applications and effective utilization of solar energy [10]. Hence, there is a significant need to establish more highly active and stable visible light-responsive photocatalysts.

Metal oxides are a class of semiconductors that have been widely studied. ZnO, TiO₂, CeO₂, and SnO₂, for example, are most commonly utilized as photocatalysts due to their stability. On the other hand, their large bandgap energies are the fundamental obstacle to deploying them as photocatalysts, which only allow for absorbance in the ultraviolet

region [11,12]. Among semiconductor photocatalysts, metal-organic frameworks (MOFs) are a promising subclass of porous crystalline materials made up of organic linkers and metal nodes (metal ions or clusters) [13].

MOFs have recently drawn increasing attention in the photocatalysis field due to their high surface area, diverse topology, and easily modifiable porous structure [14,15]. The unique properties of MOFs arranged in a crystalline lattice are different from those of regular inorganic semiconductors [10]. As an example, MIL-125 [16], MIL-101 (Cr) [17], UAEU-50 [18], and MIL-100 (Fe) [19] exhibit strong photocatalytic activity when exposed to visible light, consistent with their band gap energies of 3.24 eV, 2.28 eV, 3.0 eV, and 2.17 eV, respectively. As a result, there has been intensive research on the development of new synthetically challenging MOFs that initiate various transformations, such as photocatalytic CO₂ reduction [20], hydrogenation [21], CO₂ conversion reactions [18,22], and different organic reactions [23].

Despite the above-mentioned advantages of MOF materials, their photocatalytic efficiency remains a challenge. To overcome such drawbacks, a number of strategies have been developed to improve the photocatalytic performance of MOFs for different applications, such as synthesizing mixed metal centers [24,25], mixed ligands [26], ligand functionalization [27], metal ions immobilization [28], MOF or COF coupling [29,30], semiconductor coupling [31], adding magnetic materials, surface modification using metal nanoparticles [32], carbon-based materials [31], and dye sensitization [33]. These techniques have been used to increase MOFs' ability to absorb visible light, achieve efficient separation and transfer of charge carriers, and increase the degree of recyclability [10,12].

For diverse applications of MOFs, one of the major concerns is the stability of the targeted MOF, which includes thermal, chemical, and mechanical stability. In particular, the chemical stability of MOFs in solvents, e.g., moisture, aqueous solutions, acids, and base environments. Great efforts have been made to develop strategies to boost the stability of MOFs [34]. In terms of photocatalytic performances, the stability of MOFs is critical for their long-term activity and reusability. The degradation of MOFs can result in a loss of their photocatalytic activity, which reduces their efficiency and performance. Therefore, understanding the stability of MOFs is essential for designing and developing efficient photocatalysts for various applications.

Improving the functionalities of MOF frameworks, such as tuning the nature and size of the organic linkers used, will help to target diverse applications [35–37]. It is worth mentioning that controlling the properties of organic linkers, such as type, length, flexibility, and symmetry, will control the pore size and internal chemical functionality of the pores, making them hydrophobic, hydrophilic, and more able to adsorb specific molecules [38–41]. Therefore, accurate organic linker selection is crucial. In particular, the use of mixed linkers can lead to flexible, porous frameworks with various topologies and functionalities. In mixed-linker MOFs, modulating dimensionality, pore size, surface area, reactivity, and loading capacity would only require changing the linker structure, size, and functional groups [40–42]. For example, one of the first mixed linker MOFs was prepared by Kim and his group upon mixing different diamine and dicarboxylate ligands to alter the original [Zn₂(1,4-bdc)₂(dabco)] MOF, which enhanced the properties of this MOF [43].

Bipyridines are a group of attractive organic ligands that have been widely applied in the production of several metal complexes with significant potential use in a variety of applications, including therapeutics [44], C–H borylation, oxidation reactions, photocatalysis for CO₂ reduction, water splitting, luminescence sensors, energy storage organic reactions, solar cell applications, and catalysis [44,45].

This nitrogen donor-based ligand has been often used in the development of catalytic systems for chemical synthesis and solar energy conversion reactions because of its flexibility of functionalization, strong redox stability, and ability to coordinate with a variety of metal ions [46]. More recently, Manna and co-workers showed in several studies that the addition of simple bipyridine ligands to UiO-type MOFs is an effective method for stabilizing homogeneous catalysts, affords a significantly increased catalytic

activity, and even results in high catalytic performance that cannot be obtained with the unmodified UiO-MOF [46,47].

MOFs-based bipyridine ligands showed efficient light harvesting performance in the number of photocatalytic reactions [48–50]. In this sense, Lin and his group synthesized six stable UiO-67 MOFs containing bipyridine ligand and mixed precious metals using a mix-and-match synthetic method. Those MOFs were used in different applications such as catalytic water oxidation, photochemical CO₂ reduction, and photocatalytic organic transformations such as aerobic thioanisole oxidation, aerobic amine coupling, and the aza-Henry reaction. These heterogeneous catalysts can facilitate catalyst reuse and recycling [49].

Therefore, MOFs created from manganese, one of the most abundant metals, have demonstrated effective catalytic activity toward different photocatalytic reactions, such as CO₂ reduction [18,51], methylene blue (MB) degradation [52], and hydrogen generation [53].

Herein, we report the synthesis of two related manganese (II)-based MOFs. Mn^{II}₃(tp)_{6/2}(bpy)₂(dmf) and [Mn₂(tpa)₂(dmf)₂] were synthesized according to previous methods, and their stabilities and photoactivates were examined and compared. To the best of our knowledge, no research has been reported on using these MOFs as photocatalysts.

2. Results and Discussion

2.1. Structures Details

In this study, we selected two related manganese (II)-based MOFs: Mn^{II}₃(tp)_{6/2}(bpy)₂(dmf) and [Mn₂(tpa)₂(dmf)₂]. In 2008, Mn^{II}₃(tp)_{6/2}(bpy)₂(dmf) was first synthesized by Lu and co-workers [54]. Mn^{II}₃(tp)_{6/2}(bpy)₂(dmf) has a 2D framework structure showing a monoclinic crystal system with parameters of $a = 18.38 \text{ \AA}$, $b = 25.73 \text{ \AA}$, $c = 9.91 \text{ \AA}$ and angles of $\alpha = 90^\circ$, $\beta = 91.45^\circ$, $\gamma = 90^\circ$. Mn^{II}₃(tp)_{6/2}(bpy)₂(dmf), consisting of a Mn atom as a metal node and two linkers, 2,2'-bipyridyl (BPY), and benzene dicarboxylic acid (BDC). The Mn trinuclear cluster consists of three Mn atoms in a linear arrangement with a distance of 3.266 Å between each Mn atom. The middle Mn atom binds to six BDC linkers through carboxylate groups, while each of the two terminal Mn atoms binds to three different BDC linkers and one BPY linker (Figure 1A). On the other hand, Ladrak et al. synthesized Mn₂(tpa)₂(dmf)₂ with a 3D framework structure using Mn and one organic linker, BDC [55]. Mn₂(tpa)₂(dmf)₂ has a monoclinic crystal system with parameters $a = 13.414 \text{ \AA}$, $b = 10.162 \text{ \AA}$, $c = 17.653 \text{ \AA}$ and angles of $\alpha = 90^\circ$, $\beta = 90.21^\circ$, $\gamma = 90^\circ$. The Mn central atom adopts an octahedral coordination environment by binding to five oxygens from different BDC linkers and one oxygen from dimethylformamide solvent (Figure 1B).

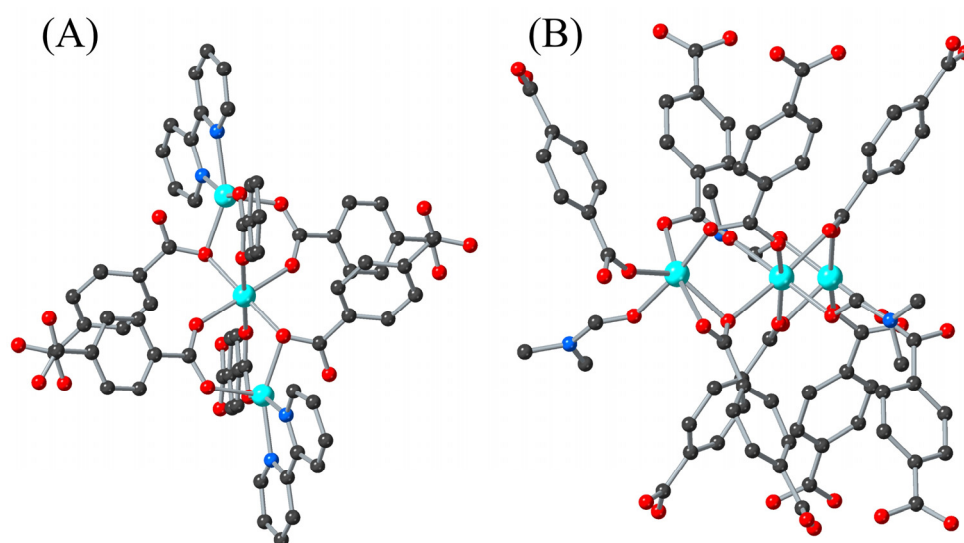


Figure 1. Crystal structure of Mn^{II}₃(tp)_{6/2}(bpy)₂(dmf) (A) and Mn₂(tpa)₂(dmf)₂ MOF (B). Atom color: O—red; C—grey; N—blue; Mn—cyan.

2.2. Powder X-ray Diffraction (PXRD)

To confirm the phase structure and purity of the prepared photocatalysts, PXRD spectra for the two MOFs ($\text{Mn}^{\text{II}}_3(\text{tp})_{6/2}(\text{bpy})_2 \cdot (\text{dmf})$ and $\text{Mn}_2(\text{tpa})_2(\text{dmf})_2$) were obtained (Figure 2). Comparing the PXRD pattern of the prepared MOFs with the simulated pattern obtained from SC-XRD matched the previously reported pattern [54,55]. In the case of $\text{Mn}^{\text{II}}_3(\text{tp})_{6/2}(\text{bpy})_2 \cdot (\text{dmf})$, some peaks were missing, which might have been a result of the preferred orientation that is typical for 2D MOFs (Figure 2) [56–58]. According to Figure 2, the peaks for synthesized $\text{Mn}_2(\text{tpa})_2(\text{dmf})_2$ are in good agreement with the previous study [55], which proved that prepared $\text{Mn}_2(\text{tpa})_2(\text{dmf})_2$ was successfully and purely synthesized. The synthesized $\text{Mn}_2(\text{tpa})_2(\text{dmf})_2$ and $\text{Mn}^{\text{II}}_3(\text{tp})_{6/2}(\text{bpy})_2 \cdot (\text{dmf})$ exhibited good crystallinity, as shown by the sharp intensities of the diffraction peaks.

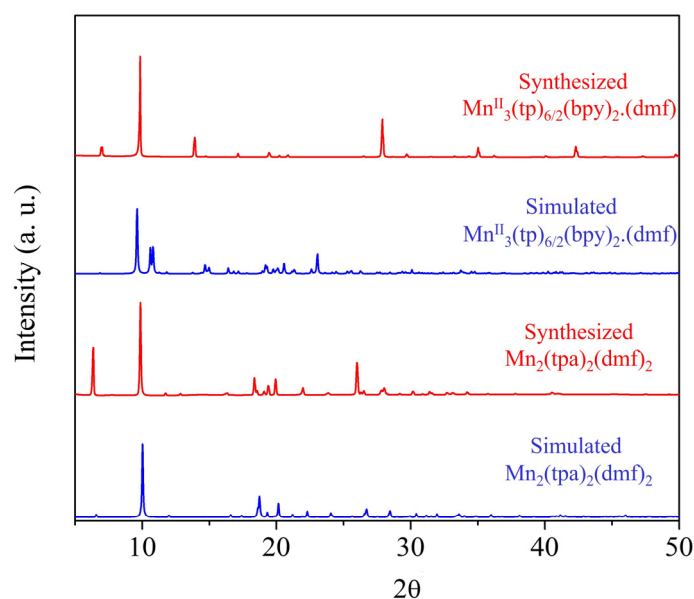


Figure 2. PXRD pattern of synthesized and simulated $\text{Mn}^{\text{II}}_3(\text{tp})_{6/2}(\text{bpy})_2 \cdot (\text{dmf})$ and $\text{Mn}_2(\text{tpa})_2(\text{dmf})_2$ MOF.

2.3. Scanning Electron Microscope (SEM) and Energy-Dispersive X-ray Spectroscopy (EDX)

The SEM images of activated $\text{Mn}^{\text{II}}_3(\text{tp})_{6/2}(\text{bpy})_2 \cdot (\text{dmf})$ showed cubic-like crystals with sizes larger than $40 \mu\text{m}$ (Figure 3A). Additionally, EDX analysis showed the sample's expected elemental composition, i.e., manganese, carbon, nitrogen, and oxygen, since those are the only elements found in this framework (Supporting Materials, SM, Figure S1, and Table S1) with no impurity elements present in the sample. The reported $\text{Mn}_2(\text{tpa})_2(\text{dmf})_2$ also showed a needle-shaped morphology (Figure 3B), and EDX analysis confirmed the presence of the same atoms (Supporting Materials, SM, Figure S2, and Table S2). It is worth mentioning that the carbon and oxygen contents cannot be correlated directly to the exact percent in each sample, since carbon tape is used in measuring the EDX of the samples in the presence of atmospheric oxygen. Nonetheless, the constituent composition was correctly matched with the expected formulas.

2.4. UV–Vis Diffuse Reflectance Spectroscopy (UV–Vis DRS)

The band gaps of both MOFs were determined using the relationship between the wavelength and reflected light intensity from DRS using the Tauc plot method and Equation (1).

$$(\alpha h\nu)^{1/n} = A (h\nu - E_g) \quad (1)$$

α , h , and ν are the absorption coefficient, Planck's constant, and light frequency, respectively. The n value is characteristic of the semiconductor transition ($n = 1/2$ for a direct allowed transition), A is a proportionality constant, and E_g is the measured band

gap energy. As illustrated in Figure 4, A, the band gap energy was determined by plotting $(h\nu)$ vs. $(\alpha h\nu)^2$. As a result, the synthesized $\text{Mn}^{\text{II}}_3(\text{tp})_{6/2}(\text{bpy})_2 \cdot (\text{dmf})$ had a band gap of 2.5 eV and exhibited strong visible light absorption. Furthermore, the diffuse reflectance data exhibit a peak in the visible light region starting at 492 nm, which confirms the ability of the photocatalyst to absorb visible light (Supporting Materials, SM, Figure S3A). This is attributed to the enhanced light harvesting capability of such an auxiliary ligand, i.e., the bipyridine, resulting in lower band gap energy compared to pristine material without the bipyridine ligand, i.e., $\text{Mn}_2(\text{tpa})_2(\text{dmf})_2$ MOF. On the other hand, the band gap for the $\text{Mn}_2(\text{tpa})_2(\text{dmf})_2$ MOF is 3.16 eV, which also shows strong absorption in the visible light region (Figure 4B). Additionally, the $\text{Mn}_2(\text{tpa})_2(\text{dmf})_2$ MOF absorbs light at approximately 392 nm, closer to the lower end of the visible light, as shown in the diffuse reflectance spectrum (Supporting Materials, SM, Figure S3B).

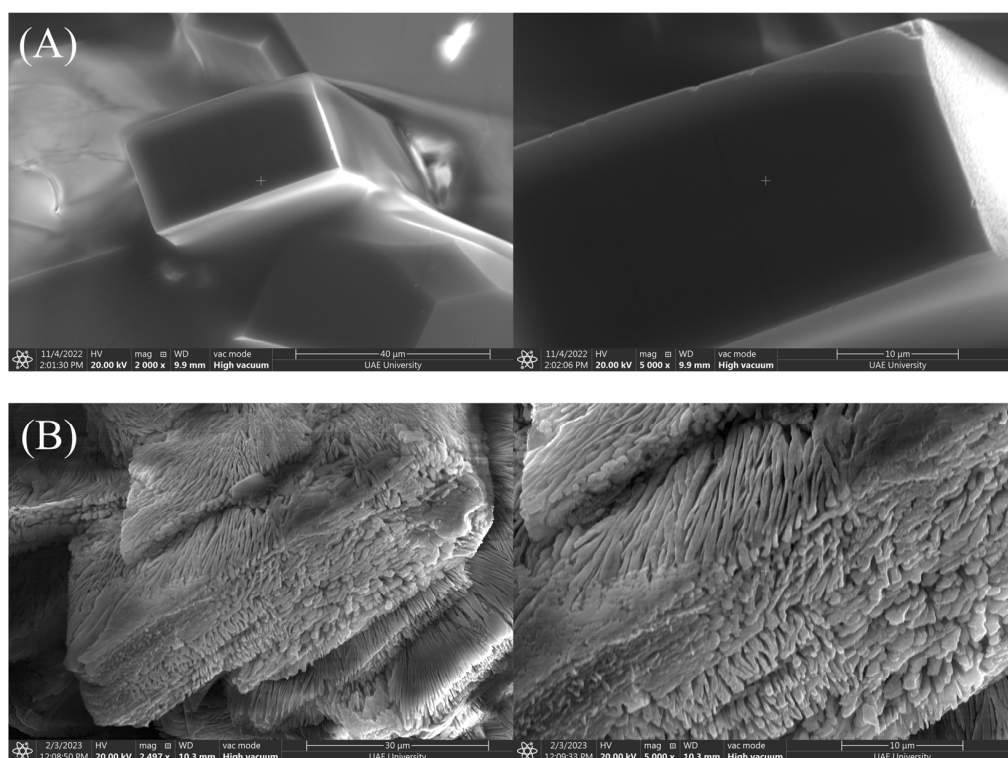


Figure 3. SEM images of $\text{Mn}^{\text{II}}_3(\text{tp})_{6/2}(\text{bpy})_2 \cdot (\text{dmf})$ (A) and $\text{Mn}_2(\text{tpa})_2(\text{dmf})_2$ MOF (B).

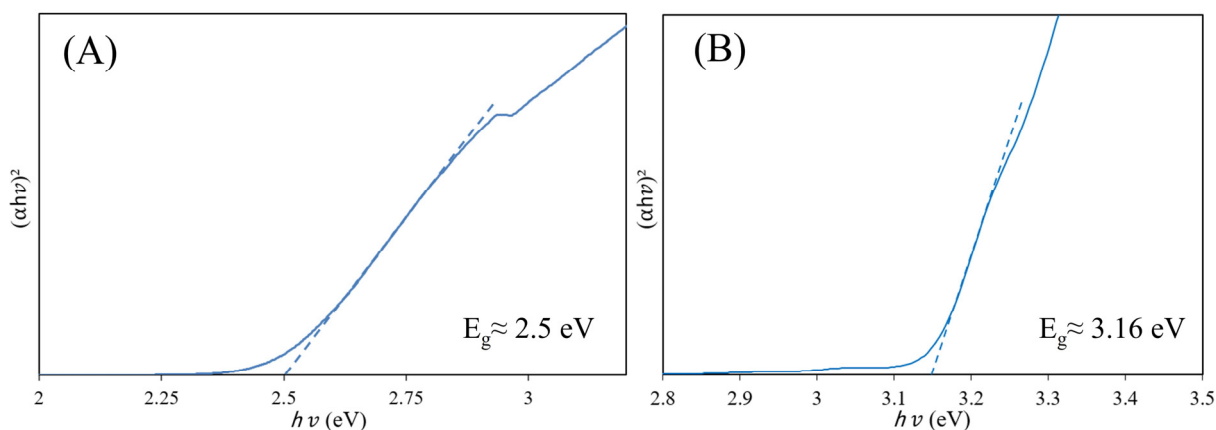


Figure 4. Tauc plot of $\text{Mn}^{\text{II}}_3(\text{tp})_{6/2}(\text{bpy})_2 \cdot (\text{dmf})$ (A) and $\text{Mn}_2(\text{tpa})_2(\text{dmf})_2$ (B); the band gap was calculated by the intercept of the line with the x -axis.

2.5. Thermal Gravimetric Analysis (TGA)

Thermal gravimetric analysis under nitrogen gas was used to investigate the thermal stability of $\text{Mn}^{\text{II}}_3(\text{tp})_{6/2}(\text{bpy})_2(\text{dmf})$ between 25 °C and 600 °C (Supporting Materials, SM, Figure S4). The 5.53 mg of $\text{Mn}^{\text{II}}_3(\text{tp})_{6/2}(\text{bpy})_2(\text{dmf})$ was decomposed in two steps. At 160 °C, the first weight loss started, and 9% of the sample was lost due to trapped DMF molecules in the pores of the $\text{Mn}^{\text{II}}_3(\text{tp})_{6/2}(\text{bpy})_2(\text{dmf})$ framework. The second step was then observed between 430 °C and 600 °C, with a major drop in weight (loss of 71%) as a result of the decomposition of the organic linkers, i.e., bipyridine and benzene dicarboxylic acid. The remaining 20% mass is a formation of manganese oxide (Mn_2O_3), which is the outcome of the decomposition of $\text{Mn}^{\text{II}}_3(\text{tp})_{6/2}(\text{bpy})_2(\text{dmf})$. However, $\text{Mn}_2(\text{tpa})_2(\text{dmf})_2$ started to decompose at 150 °C, which could be attributed to the DMF solvent. Following this step, there are two degradation steps at 270 °C and 400 °C when it converts to manganese oxide (Mn_2O_3) (Supporting Materials, SM, Figure S4). The production of Mn_2O_3 for both MOFs was confirmed using PXRD and the Match3! software program, as shown in Figure S5.

2.6. Stability Test

The chemical stability of $\text{Mn}^{\text{II}}_3(\text{tp})_{6/2}(\text{bpy})_2(\text{dmf})$ was tested in several organic solvents, such as acetonitrile, ethanol, methanol, and acetone. Upon comparing the PXRD patterns of the four samples with that of the pure activated MOF, it was clear that $\text{Mn}^{\text{II}}_3(\text{tp})_{6/2}(\text{bpy})_2(\text{dmf})$ exhibits great stability in all the aforementioned solvents after 7 days of permanent exposure to the solvent system (Figure 5A). A similar test was performed for the pristine $\text{Mn}_2(\text{tpa})_2(\text{dmf})_2$ to compare its stability with that of the $\text{Mn}^{\text{II}}_3(\text{tp})_{6/2}(\text{bpy})_2(\text{dmf})$. Interestingly, $\text{Mn}_2(\text{tpa})_2(\text{dmf})_2$ showed less stability than $\text{Mn}^{\text{II}}_3(\text{tp})_{6/2}(\text{bpy})_2(\text{dmf})$ in most of the solvents, whereas it totally decomposed in acetonitrile and acetone after only 2 days (Figure 5B). The PXRD patterns of $\text{Mn}_2(\text{tpa})_2(\text{dmf})_2$ in all solvents were different than the synthesized pristine one; the peak at approximately 5 degrees disappeared, whereas a new peak at 15 degrees appeared, indicating a difference in the structure of $\text{Mn}_2(\text{tpa})_2(\text{dmf})_2$. However, acetonitrile was used in the photocatalytic reaction; therefore, it was difficult to evaluate $\text{Mn}_2(\text{tpa})_2(\text{dmf})_2$ in such a solvent environment.

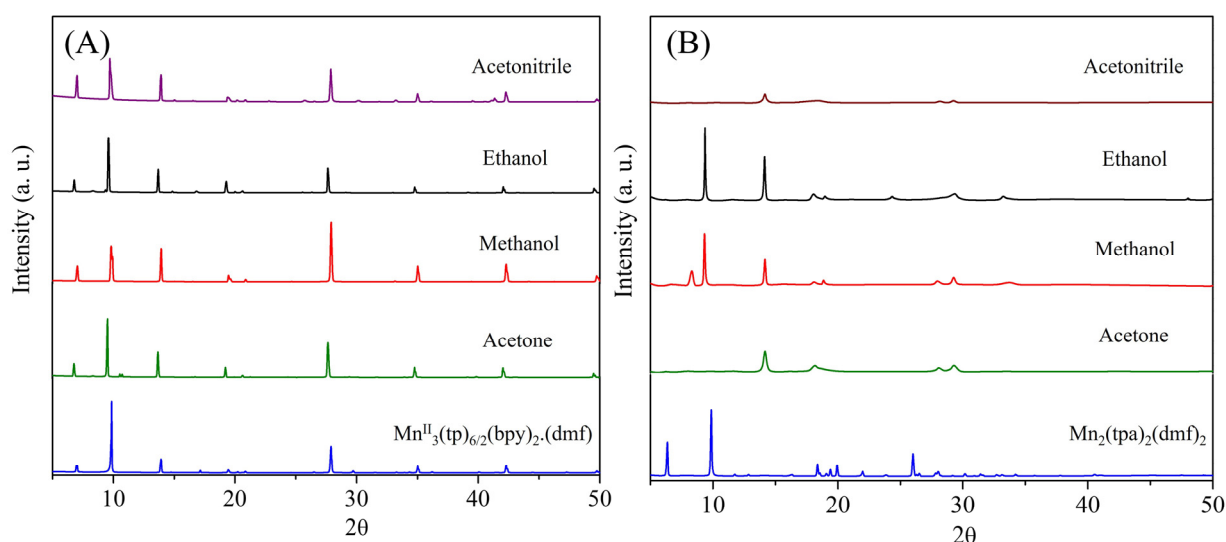


Figure 5. Chemical stability test of $\text{Mn}^{\text{II}}_3(\text{tp})_{6/2}(\text{bpy})_2(\text{dmf})$ (A) and $\text{Mn}_2(\text{tpa})_2(\text{dmf})_2$ (B) proven by the PXRD pattern in several solvents (10 mg sample was immersed in 5 mL of each solvent).

2.7. Fourier-Transform Infrared (FT-IR) Spectroscopy

As shown in Figure 6, the coordination interaction and binding mode between the starting material, benzene dicarboxylic acid (BDC), and manganese were confirmed using FT-IR spectroscopy. Upon comparing the red IR spectrum of $\text{Mn}^{\text{II}}_3(\text{tp})_{6/2}(\text{bpy})_2(\text{dmf})$ with

the blue IR spectrum of BDC, in $\text{Mn}^{\text{II}}_3(\text{tp})_{6/2}(\text{bpy})_2 \cdot (\text{dmf})$, the IR band at 3474 cm^{-1} indicated that the O-H group for BDC disappeared, which suggests the chelation of manganese with the hydroxyl group of BDC. Furthermore, a slight shift was observed in the carboxylic band (C=O) from 1684 cm^{-1} (BDC) to 1601 cm^{-1} $\text{Mn}^{\text{II}}_3(\text{tp})_{6/2}(\text{bpy})_2 \cdot (\text{dmf})$, which further supports the -OH group as the binding site. Compared to $\text{Mn}_2(\text{tpa})_2(\text{dmf})_2$, this shift is higher due to Mn binding to bipyridine. A slight shift was observed in $\text{Mn}_2(\text{tpa})_2(\text{dmf})_2$ in the carboxylic band (C=O) from 1684 cm^{-1} (BDC) to 1654 cm^{-1} to prove the chelation between the hydroxyl group in BDC and the manganese metal ion.

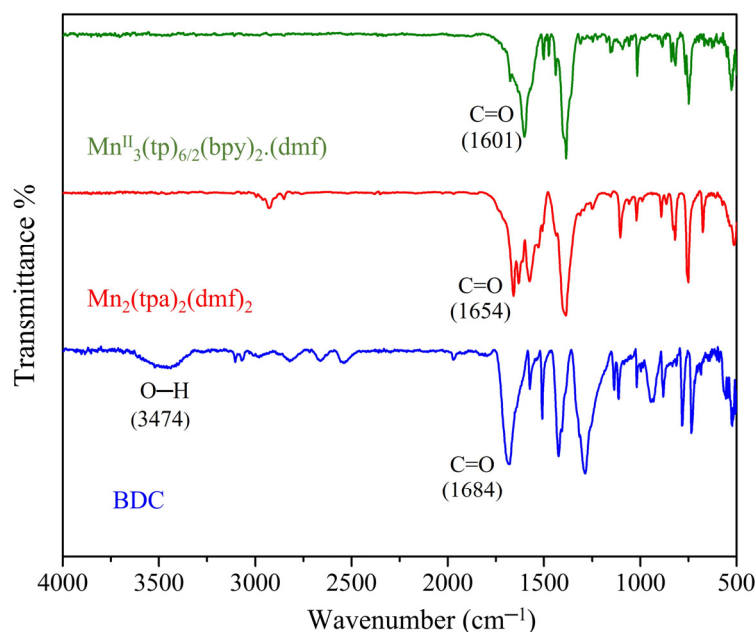


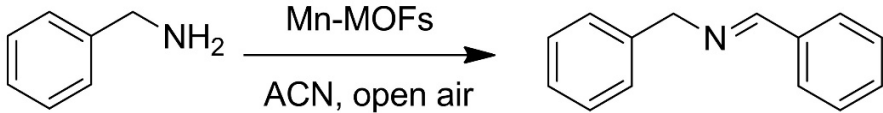
Figure 6. FTIR spectra of $\text{Mn}^{\text{II}}_3(\text{tp})_{6/2}(\text{bpy})_2 \cdot (\text{dmf})$, $\text{Mn}_2(\text{tpa})_2(\text{dmf})_2$ and BDC.

2.8. $\text{Mn}^{\text{II}}_3(\text{tp})_{6/2}(\text{bpy})_2 \cdot (\text{dmf})$ Photocatalytic Activity

The photocatalytic activity of $\text{Mn}^{\text{II}}_3(\text{tp})_{6/2}(\text{bpy})_2 \cdot (\text{dmf})$ was investigated based on its band gap value of $\text{Mn}^{\text{II}}_3(\text{tp})_{6/2}(\text{bpy})_2 \cdot (\text{dmf})$, which is 2.5 eV using a simulated visible light halogen lamp light source. An oxidative coupling reaction of benzylamine was carried out as a model photocatalytic reaction. A 90% conversion yield with $\text{Mn}^{\text{II}}_3(\text{tp})_{6/2}(\text{bpy})_2 \cdot (\text{dmf})$ was obtained. On the other hand, $\text{Mn}_2(\text{tpa})_2(\text{dmf})_2$ was unstable and decomposed in acetonitrile when used as the solvent for the photocatalytic reaction because the reaction was performed under neat conditions, which gave a very low yield of 9%. $^1\text{H-NMR}$, $^{13}\text{C-NMR}$, and FTIR were used to confirm the isolated product, N-benzylidenebenzylamine (Supporting Materials, SM, Figures S6 and S7). The same procedure was used for all control experiments, as shown in Table 1. The NMR shifts obtained for the product were as follows: $^1\text{H-NMR}$ (400 MHz, CDCl_3): δ 8.40 (s, 1H), 7.80–7.77 (m, 2H), 7.43–7.41 (m, 3H), 7.35–7.34 (m, 4H), 7.29–7.26 (m, 1H), 4.83 (s, 2H), and $^{13}\text{C-NMR}$ (400 MHz, CDCl_3): δ 162, 139.23, 136.09, 130.78, 128.61, 128.49, 128.27, 127.98, 126.99, 65.06.

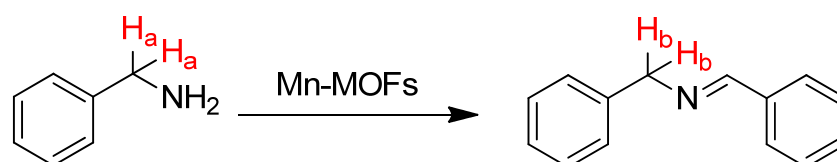
Furthermore, a variety of control experiments were carried out to investigate other reaction conditions and prove that the reaction is photocatalytic in nature, as listed in Table 1. The percent yields were determined following Equation (2) by comparing the $^1\text{H-NMR}$ integral of the -NCH protons of the starting material ($^1\text{H}_a$) with the relevant protons in the product ($^1\text{H}_b$) (Scheme 1) [59].

$$\text{Conversion} = \frac{1_{\text{Hb}}}{(1_{\text{Ha}} + 1_{\text{Hb}})} \quad (2)$$

Table 1. Photocatalytic oxidation of benzylamine using the Mn-MOFs photocatalysts under different conditions.


Entry	Control Conditions	Conversion Yield (%)
I	5 mg Mn ^{II} ₃ (tp) _{6/2} (bpy) ₂ ·(dmf), light, acetonitrile (ACN)	90
II	5 mg Mn ^{II} ₃ (tp) _{6/2} (bpy) ₂ ·(dmf), light, no solvent	2
III	Mn ^{II} ₃ (tp) _{6/2} (bpy) ₂ ·(dmf), no light, no heat	Nil
IV	Mn ^{II} ₃ (tp) _{6/2} (bpy) ₂ ·(dmf), heat, no light	2
V	Heat, no light, no Mn ^{II} ₃ (tp) _{6/2} (bpy) ₂ ·(dmf)	Nil
VI	light, no Mn ^{II} ₃ (tp) _{6/2} (bpy) ₂ ·(dmf)	Nil
VII	5 mg Mn ₂ (tpa) ₂ (dmf) ₂ , light, no solvent	9

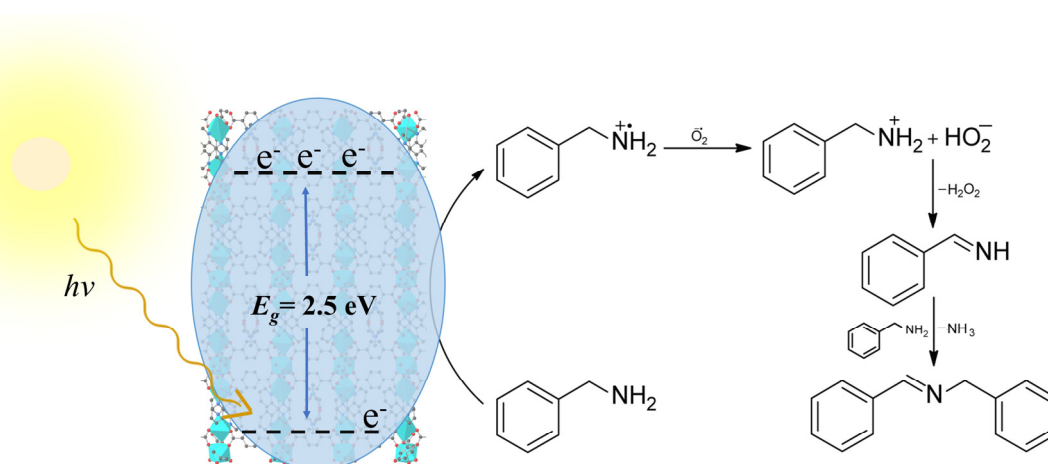
Reaction optimum conditions: 0.5 mmol (51 μL) benzylamine, 6.4 × 10⁻³ mmol photocatalyst, 2 mL acetonitrile (ACN), open air, irradiated for 24 h.

**Scheme 1.** Synthesis of N-benzylidenebenzylamine.

The highest yield obtained was 90% when the reaction was conducted in 2 mL acetonitrile in the open air, while the yield was only 2% in the absence of solvent (neat condition). It has been experimentally proven that polar solvents can enhance imine formation conversion, which explains the low observed yield under neat reaction conditions [60]. The acetonitrile solvent was chosen as the optimum medium among other solvents that were experimentally examined by Sun and his group [61]. The reaction was also performed under no light irradiation (entry III), which showed no conversion, proving that this reaction is photocatalytic in nature. Since the halogen lamp used has a heating effect, to study the effect of heat in the absence of light irradiation, a test was conducted in the dark at 70 °C in the presence of the photocatalyst (entry IV) and without the photocatalyst (entry V), which gave yields of 2% and 0%, respectively, indicating that heat has no effect on the reaction performance. Entries V and VI show no conversion in the absence of the photocatalyst, which supports the photocatalytic activity of the Mn^{II}₃(tp)_{6/2}(bpy)₂·(dmf). The photoactivity performance of Mn₂(tpa)₂(dmf)₂ was tested under neat conditions due to the instability of this MOF in ACN solvent, which yielded 9% (entry VII). After the photocatalytic run, an attempt was made to recycle the photocatalysts by filtering; however, the crystalline quality of the powder material was difficult to retain and was lost during filtration.

Scheme 2 showed the proposed mechanism of aerobic oxidative coupling of benzylamine using Mn^{II}₃(tp)_{6/2}(bpy)₂·(dmf) started when the photocatalyst was irradiated with simulated visible light, and the electron was excited and moved to the conduction band (CB), leaving a hole behind it in the valence band (VB). The photoexcited electron reacted with the atmospheric oxygen molecules to produce the O₂^{•-} radical, which was confirmed previously by electron spin resonance (EPR) measurements [62–64]. The photoinduced hole in the VB oxidized the adsorbed benzylamine, producing an aminium radical cation intermediate. Then, the intermediate reacted with the O₂^{•-} radical to form phenylmethanamine (Ph-CH₂-NH₂) through hydrogen-atom abstraction, producing H₂O₂ and Ph-CH=NH as a result [63]. The subsequent dissociation of H₂O₂ to •OH radicals triggers oxidized

benzylamine to form imine, which as a result reacts with free benzylamine to produce the N-benzylidenebenzylamine product and releases ammonia [64].



Scheme 2. Proposed mechanism of benzylamine coupling over $\text{Mn}^{\text{II}}_3(\text{tp})_{6/2}(\text{bpy})_2 \cdot (\text{dmf})$. Radical cation is presented by (+·) and radical anion is presented by (·-).

3. Experimental Section

3.1. Materials and General Procedures

Manganese (II) nitrate tetrahydrate ($\text{Mn}(\text{NO}_3)_2 \cdot 4\text{H}_2\text{O}$), 2,2'-bipyridyl (BPY), benzene dicarboxylic acid (BDC), anhydrous dimethylformamide (DMF), dichloromethane (DCM), acetone, and acetonitrile (ACN) were received from Sigma-Aldrich (St. Louis, MO, USA) and used without purification. Powder X-ray diffraction (PXRD, Neu-Isenburg, Germany) measurements were performed by a Rigaku MiniFlex benchtop X-ray diffractometer equipped with a CuK radiation tube ($\lambda = 1.542 \text{ \AA}$) at 40 kV with an operating rate of 2° min^{-1} in the range of $3\text{--}50^\circ 2\theta$. Scanning electron microscopy (SEM, Waltham, MA, USA) images were captured with a Quattro ESEM instrument operated with a 30 kV accelerating voltage and high vacuum. For the EDX analysis, a Quattro ESEM was used with an energy-dispersive X-ray (EDX detector, Waltham, MA, USA). To determine the band gap energies, UV–Vis diffuse reflection spectroscopy (DRS, Kyoto, Japan) was conducted using a Shimadzu UV–3600 UV–Vis diffuse reflectance spectrophotometer in the 200 nm to 800 nm wavelength range with a baseline sample of barium sulfate. Thermogravimetric analysis (TGA, Kyoto, Japan) was performed in a Shimadzu TGA-50 analyzer using an aluminum pan sample container under nitrogen gas with a 50 mL min^{-1} flow rate. The FT-IR spectra of the prepared MOFs and the final product of the photocatalytic reaction were produced using a Thermo Nicolet Nexus 470 FT-IR spectrophotometer (Santa Clara, CA, USA) by using the potassium bromide (KBr) pellet method. The measured spectral range was 4000 cm^{-1} to 500 cm^{-1} , with an average spectral resolution of 2 cm^{-1} . Each FTIR spectrum was automatically subtracted from the initial background (air) spectrum. To obtain the $^1\text{H-NMR}$ and $^{13}\text{C-NMR}$ spectra of the generated photocatalytic compounds, a Varian-400 MHz instrument (Palo Alto, CA, USA) was used at room temperature with a ppm reference and TMS standard. CDCl_3 was used as the deuterated solvent in all samples.

3.2. Synthesis of $\text{Mn}^{\text{II}}_3(\text{tp})_{6/2}(\text{bpy})_2 \cdot (\text{dmf})$

$\text{Mn}^{\text{II}}_3(\text{tp})_{6/2}(\text{bpy})_2 \cdot (\text{dmf})$ was synthesized by a solvothermal method with modified conditions as reported by Lu et al. [54] $\text{Mn}(\text{NO}_3)_2 \cdot 4\text{H}_2\text{O}$ (8.9 mg, 0.05 mmol), BPY (15.6 mg, 0.1 mmol), and BDC (16.7 mg, 0.1 mmol) were added to a 75-mL Pyrex-sealed tube with 10 mL of DMF solvent. Then, the sealed tube was tightly closed and placed in a preheated oven at 100°C for 24 h. After the reaction was complete, the yellow crystals were washed with acetone three times. For activation, the acetone solvent was removed, and the crystals were dried at 100°C in a vacuum oven for 24 h.

3.3. Synthesis of $Mn_2(tpa)_2(dmf)_2$ MOF

$Mn_2(tpa)_2(dmf)_2$ was prepared following the same procedure reported by Ladrak et al. [55]. The reaction was attained in a 75-mL Pyrex-sealed tube by dissolving BDC (99 mg, 0.5475 mmol) and $Mn(NO_3)_2 \cdot 4H_2O$ (92 mg, 0.365 mmol) in 10 mL DMF solvent. The reaction was placed in a preheated oven for 24 h at 120 °C. Colorless crystals were isolated, washed with DCM, and dried under vacuum for 24 h at 50 °C.

3.4. Photocatalytic Activity

Photocatalytic testing was conducted under normal atmospheric “open air” conditions. In a typical procedure, 5.0 mg (0.006 mmol) of the photocatalyst and 51 μ L (0.50 mmol) of benzylamine in 2 mL of acetonitrile were added to a 25-mL round-bottom flask attached to a condenser. The reaction was stirred and subjected to a 400-W halogen lamp (OSRAM HALOLINE, Munich, Germany) operating in the wavelength range of 380–780 nm for 24 h without using a cutoff filter. After that, the photocatalyst was washed using acetonitrile and removed by syringe filtering. The solvent was then removed by a rotary evaporator, and a pale-yellow oil was produced. The pure final product was characterized using 1H -NMR, ^{13}C -NMR, and IR techniques.

4. Conclusions

$Mn^{II}_3(tp)_{6/2}(bpy)_2 \cdot (dmf)$ and $Mn_2(tpa)_2(dmf)_2$ were successfully synthesized with BDC and manganese metal for $Mn_2(tpa)_2(dmf)_2$ and with mixed ligands BDC and BPY for $Mn^{II}_3(tp)_{6/2}(bpy)_2 \cdot (dmf)$. The stability of these MOFs was tested by different experiments and characterization techniques, which showed that the mixed ligand MOF, i.e., $Mn^{II}_3(tp)_{6/2}(bpy)_2 \cdot (dmf)$, has higher chemical stability. In addition to its stability, the band gap proved that $Mn^{II}_3(tp)_{6/2}(bpy)_2 \cdot (dmf)$ has a lower band gap (2.5 eV), making it a promising candidate as a photocatalyst under visible light irradiation. $Mn^{II}_3(tp)_{6/2}(bpy)_2 \cdot (dmf)$ showed higher photocatalytic performance under mild reaction conditions than $Mn_2(tpa)_2(dmf)_2$. The advantages of using the mixed ligand strategy presented in this report open opportunities for a synthesized variety of mixed ligand MOF materials with enhanced physical and optical properties suited for diverse applications. In summary, the presented bipyridine mixed ligands metal-organic framework showed enhanced chemical and thermal stability and photoresponse, and the optical absorption spectra confirm that the incorporation of bipyridine improves the visible light absorption property of the metal-organic framework. The overall investigation implements mixed ligands as potential future light-harvesting materials for manifold applications.

Supplementary Materials: The following supporting information can be downloaded at: <https://www.mdpi.com/article/10.3390/catal13030613/s1>, Figure S1: EDX spectrum of $Mn^{II}_3(tp)_{6/2}(bpy)_2 \cdot (dmf)$ with presence of elements Mn, N, C, and O in the sample; Figure S2: EDX spectrum of $Mn_2(tpa)_2(dmf)_2$ showing the elements Mn, C, O, and N in the sample; Figure S3: The diffuse reflectance spectrum of $Mn^{II}_3(tp)_{6/2}(bpy)_2 \cdot (dmf)$ (A) and $Mn_2(tpa)_2(dmf)_2$ (B); Figure S4: Thermogravimetric analysis of $Mn^{II}_3(tp)_{6/2}(bpy)_2 \cdot (dmf)$ and $Mn_2(tpa)_2(dmf)_2$ under nitrogen flow and 10 °C min^{-1} heating rate; Figure S5: The PXRD pattern of obtained Mn_2O_3 from calcinated Mn-MOFs through TGA analysis; Figure S6: 1H -NMR (A) and ^{13}C -NMR (B) Spectra of *N*-benzylidenebenzylamine product; Figure S7: FT-IR spectrum of *N*-benzylidenebenzylamine product; Table S1: Atomic percentages of $Mn^{II}_3(tp)_{6/2}(bpy)_2 \cdot (dmf)$ and Table S2: Atomic percentages of $Mn_2(tpa)_2(dmf)_2$.

Author Contributions: Conceptualization, A.A. and L.A.S.; methodology, L.A.S., A.S.A. and R.H.A.; software, L.A.S., A.S.A., R.H.A. and A.A.; validation, A.A.; formal analysis, L.A.S.; investigation, L.A.S., A.S.A. and R.H.A.; resources, A.A.; data curation, L.A.S., A.S.A., R.H.A. and A.A.; writing—original draft preparation, L.A.S. and A.A.; writing—review and editing, L.A.S., R.H.A. and A.A.; visualization, L.A.S.; supervision, A.A.; project administration, A.A.; funding acquisition, A.A. All authors have read and agreed to the published version of the manuscript.

Funding: This work was funded by the National Water and Energy Centre (UAUEU, Grant no. 31R238, Ahmed Alzamy).

Data Availability Statement: The data generated during and/or analysed during the study are available from the corresponding author on reasonable request.

Acknowledgments: The work is financially supported by National Water and Energy Centre. The authors would like to thank Afra Alblooshi for recording the SEM images.

Conflicts of Interest: All authors certify that the submission is original work and is not under review at any other publication.

References

1. Wang, H.; Zhang, L.; Chen, Z.; Hu, J.; Li, S.; Wang, Z.; Liu, J.; Wang, X. Semiconductor Heterojunction Photocatalysts: Design, Construction, and Photocatalytic Performances. *Chem. Soc. Rev.* **2014**, *43*, 5234–5244. [[CrossRef](#)] [[PubMed](#)]
2. Zhou, R.; Ma, L.; Yang, X.; Cao, J. Recent Advances in Visible-Light Photocatalytic Deuteration Reactions. *Org. Chem. Front.* **2021**, *8*, 426–444. [[CrossRef](#)]
3. Chen, H.; Wan, K.; Zheng, F.; Zhang, Z.; Zhang, Y.; Long, D. Mechanism Insight into Photocatalytic Conversion of Lignin for Valuable Chemicals and Fuels Production: A State-of-the-Art Review. *Renew. Sustain. Energy Rev.* **2021**, *147*, 111217. [[CrossRef](#)]
4. Stroyuk, O.L.; Kuchmy, S.Y. Heterogeneous Photocatalytic Selective Reductive Transformations of Organic Compounds: A Review. *Theor. Exp. Chem.* **2020**, *56*, 143–173. [[CrossRef](#)]
5. Chakhtouna, H.; Benzeid, H.; Zari, N.; Qaiss, A.E.K.; Bouhfid, R. Recent Progress on Ag/TiO₂ Photocatalysts: Photocatalytic and Bactericidal Behaviors. *Environ. Sci. Pollut. Res.* **2021**, *28*, 44638–44666. [[CrossRef](#)]
6. Bakiro, M.; Ahmed, S.H.; Alzamly, A. Cycloaddition of CO₂ to Propylene Oxide Using BiNbO₄/NH₂-MIL-125(Ti) Composites as Visible-Light Photocatalysts. *J. Environ. Chem. Eng.* **2020**, *8*, 104461. [[CrossRef](#)]
7. Bakiro, M.; Ahmed, S.H.; Alzamly, A. Investigation of the Band Gap Energy Shift and Photocatalytic Properties of Bi³⁺-Doped Ceria. *Inorg. Chem. Commun.* **2020**, *116*, 107906. [[CrossRef](#)]
8. Alzamly, A.; Bakiro, M.; Ahmed, S.H.; Sallabi, S.M.; Al Ajeil, R.A.; Alawadhi, S.A.; Selem, H.A.; Al Meshayei, S.S.M.; Khaleel, A.; Al-Shamsi, N.; et al. Construction of BiOF/BiOI Nanocomposites with Tunable Band Gaps as Efficient Visible-Light Photocatalysts. *J. Photochem. Photobiol. A Chem.* **2019**, *375*, 30–39. [[CrossRef](#)]
9. Shi, H.; Zhao, T.; Wang, J.; Wang, Y.; Chen, Z.; Liu, B.; Ji, H.; Wang, W.; Zhang, G.; Li, Y. Fabrication of G-C₃N₄/PW₁₂/TiO₂ Composite with Significantly Enhanced Photocatalytic Performance under Visible Light. *J. Alloys Compd.* **2021**, *860*, 157924. [[CrossRef](#)]
10. Wang, Q.; Gao, Q.; Al-Enizi, A.M.; Nafady, A.; Ma, S. Recent Advances in MOF-Based Photocatalysis: Environmental Remediation under Visible Light. *Inorg. Chem. Front.* **2020**, *7*, 300–339. [[CrossRef](#)]
11. Khan, M.M.; Adil, S.F.; Al-Mayouf, A. Metal Oxides as Photocatalysts. *J. Saudi Chem. Soc.* **2015**, *19*, 462–464. [[CrossRef](#)]
12. Khan, M.M.; Rahman, A.; Matussin, S.N. Recent Progress of Metal-Organic Frameworks and Metal-Organic Frameworks-Based Heterostructures as Photocatalysts. *Nanomaterials* **2022**, *12*, 2820. [[CrossRef](#)]
13. Yaghi, O.M.; O’Keeffe, M.; Ockwig, N.W.; Chae, H.K.; Eddaoudi, M.; Kim, J. Reticular Synthesis and the Design of New Materials. *Nature* **2003**, *423*, 705–714. [[CrossRef](#)]
14. Cai, G.; Yan, P.; Zhang, L.; Zhou, H.-C.; Jiang, H.-L. Metal–Organic Framework-Based Hierarchically Porous Materials: Synthesis and Applications. *Chem. Rev.* **2021**, *121*, 12278–12326. [[CrossRef](#)] [[PubMed](#)]
15. Zhao, C.; Zhou, A.; Dou, Y.; Zhou, J.; Bai, J.; Li, J.-R. Dual MOFs Template-Directed Fabrication of Hollow-Structured Heterojunction Photocatalysts for Efficient CO₂ Reduction. *Chem. Eng. J.* **2021**, *416*, 129155. [[CrossRef](#)]
16. Abdul Mubarak, N.S.; Foo, K.Y.; Schneider, R.; Abdelhameed, R.M.; Sabar, S. The Chemistry of MIL-125 Based Materials: Structure, Synthesis, Modification Strategies and Photocatalytic Applications. *J. Environ. Chem. Eng.* **2022**, *10*, 106883. [[CrossRef](#)]
17. Du, P.D.; Thanh, H.T.M.; To, T.C.; Thang, H.S.; Tinh, M.X.; Tuyen, T.N.; Hoa, T.T.; Khieu, D.Q. Metal-Organic Framework MIL-101: Synthesis and Photocatalytic Degradation of Remazol Black B Dye. *J. Nanomater.* **2019**, *2019*, 6061275. [[CrossRef](#)]
18. Siddig, L.A.; Alzard, R.H.; Nguyen, H.L.; Göb, C.R.; Alnaqbi, M.A.; Alzamly, A. Hexagonal Layer Manganese Metal–Organic Framework for Photocatalytic CO₂ Cycloaddition Reaction. *ACS Omega* **2022**, *7*, 9958–9963. [[CrossRef](#)]
19. Laurier, K.G.M.; Vermoortele, F.; Ameloot, R.; De Vos, D.E.; Hofkens, J.; Roefsaers, M.B.J. Iron(III)-Based Metal-Organic Frameworks as Visible Light Photocatalysts. *J. Am. Chem. Soc.* **2013**, *135*, 14488–14491. [[CrossRef](#)]
20. Nguyen, H.L. Reticular Materials for Artificial Photoreduction of CO₂. *Adv. Energy Mater.* **2020**, *10*, 1–23. [[CrossRef](#)]
21. Shen, Q.; Li, X.; Li, R.; Wu, Y. Application of Metal–Organic Framework Materials and Derived Porous Carbon Materials in Catalytic Hydrogenation. *ACS Sustain. Chem. Eng.* **2020**, *8*, 17608–17621. [[CrossRef](#)]
22. Alzard, R.H.; Siddig, L.A.; Alhatti, N.; Abdallah, I.; Aljabri, L.; Alblooshi, A.; Alzamly, A. Titania Derived from NH₂-MIL-125(Ti) Metal–Organic Framework for Selective Photocatalytic Conversion of CO₂ to Propylene Carbonate. *Comments Inorg. Chem.* **2022**, *43*, 1–15. [[CrossRef](#)]
23. Alzard, R.H.; Siddig, L.A.; Abdelhamid, A.S.; Alzamly, A. Visible-Light-Driven Photocatalytic Coupling of Neat Benzylamine over a Bi-Ellagate Metal–Organic Framework. *ACS Omega* **2022**, *7*, 36689–36696. [[CrossRef](#)]
24. Li, M.; Yuan, J.; Wang, G.; Yang, L.; Shao, J.; Li, H.; Lu, J. One-Step Construction of Ti-In Bimetallic MOFs to Improve Synergistic Effect of Adsorption and Photocatalytic Degradation of Bisphenol A. *Sep. Purif. Technol.* **2022**, *298*, 121658. [[CrossRef](#)]

25. Shan, C.; Zhang, X.; Ma, S.; Xia, X.; Shi, Y.; Yang, J. Preparation and Application of Bimetallic Mixed Ligand MOF Photocatalytic Materials. *Colloids Surfaces A Physicochem. Eng. Asp.* **2022**, *636*, 128108. [[CrossRef](#)]
26. Somnath; Ahmad, M.; Siddiqui, K.A. Synthesis of Mixed Ligand 3D Cobalt MOF: Smart Responsiveness towards Photocatalytic Dye Degradation in Environmental Contaminants. *J. Mol. Struct.* **2022**, *1265*, 133399. [[CrossRef](#)]
27. Chen, H.; Liu, C.; Guo, W.; Wang, Z.; Shi, Y.; Yu, Y.; Wu, L. Functionalized UiO-66(Ce) for Photocatalytic Organic Transformation: The Role of Active Sites Modulated by Ligand Functionalization. *Catal. Sci. Technol.* **2022**, *12*, 1812–1823. [[CrossRef](#)]
28. Han, W.; Shao, L.-H.; Sun, X.-J.; Liu, Y.-H.; Zhang, F.-M.; Wang, Y.; Dong, P.-Y.; Zhang, G.-L. Constructing Cu Ion Sites in MOF/COF Heterostructure for Noble-Metal-Free Photoredox Catalysis. *Appl. Catal. B Environ.* **2022**, *317*, 121710. [[CrossRef](#)]
29. Ye, Z.; Feng, S.; Wu, W.; Zhou, Y.; Wang, Y.; Dai, X.; Cao, X. Synthesis of Double MOFs Composite Material for Visible Light Photocatalytic Degradation of Tetracycline. *Solid State Sci.* **2022**, *127*, 106842. [[CrossRef](#)]
30. Lv, S.-W.; Liu, J.-M.; Li, C.-Y.; Zhao, N.; Wang, Z.-H.; Wang, S. Two Novel MOFs@COFs Hybrid-Based Photocatalytic Platforms Coupling with Sulfate Radical-Involved Advanced Oxidation Processes for Enhanced Degradation of Bisphenol A. *Chemosphere* **2020**, *243*, 125378. [[CrossRef](#)]
31. Liu, X.; Zhang, L.; Li, Y.; Xu, X.; Du, Y.; Jiang, Y.; Lin, K. A Novel Heterostructure Coupling MOF-Derived Fluffy Porous Indium Oxide with g-C₃N₄ for Enhanced Photocatalytic Activity. *Mater. Res. Bull.* **2021**, *133*, 111078. [[CrossRef](#)]
32. Lu, W.; Duan, C.; Liu, C.; Zhang, Y.; Meng, X.; Dai, L.; Wang, W.; Yu, H.; Ni, Y. A Self-Cleaning and Photocatalytic Cellulose-Fiber-Supported “Ag@AgCl@MOF-Cloth” Membrane for Complex Wastewater Remediation. *Carbohydr. Polym.* **2020**, *247*, 116691. [[CrossRef](#)] [[PubMed](#)]
33. Mahmoud Idris, A.; Jiang, X.; Tan, J.; Cai, Z.; Lou, X.; Wang, J.; Li, Z. Dye-Sensitized Fe-MOF Nanosheets as Visible-Light Driven Photocatalyst for High Efficient Photocatalytic CO₂ Reduction. *J. Colloid Interface Sci.* **2022**, *607*, 1180–1188. [[CrossRef](#)] [[PubMed](#)]
34. Ding, M.; Cai, X.; Jiang, H.L. Improving MOF Stability: Approaches and Applications. *Chem. Sci.* **2019**, *10*, 10209–10230. [[CrossRef](#)]
35. Cai, M.; Qin, L.; You, L.; Yao, Y.; Wu, H.; Zhang, Z.; Zhang, L.; Yin, X.; Ni, J. Functionalization of MOF-5 with Mono-Substituents: Effects on Drug Delivery Behavior. *RSC Adv.* **2020**, *10*, 36862–36872. [[CrossRef](#)]
36. Bahamon, D.; Anlu, W.; Builes, S.; Khaleel, M.; Vega, L.F. Effect of Amine Functionalization of MOF Adsorbents for Enhanced CO₂ Capture and Separation: A Molecular Simulation Study. *Front. Chem.* **2021**, *8*, 574–622. [[CrossRef](#)]
37. Sunder, N.; Fong, Y.Y.; Bustam, M.A.; Suhaimi, N.H. Development of Amine-Functionalized Metal-Organic Frameworks Hollow Fiber Mixed Matrix Membranes for CO₂ and CH₄ Separation: A Review. *Polymers* **2022**, *14*, 1408. [[CrossRef](#)]
38. Mulfort, K.L.; Farha, O.K.; Malliakas, C.D.; Kanatzidis, M.G.; Hupp, J.T. An Interpenetrated Framework Material with Hysteretic CO₂ Uptake. *Chem. A Eur. J.* **2010**, *16*, 276–281. [[CrossRef](#)]
39. Wang, J.H.; Li, M.; Li, D. A Dynamic, Luminescent and Entangled MOF as a Qualitative Sensor for Volatile Organic Solvents and a Quantitative Monitor for Acetonitrile Vapour. *Chem. Sci.* **2013**, *4*, 1793–1801. [[CrossRef](#)]
40. Haldar, R.; Maji, T.K. Metal-Organic Frameworks (MOFs) Based on Mixed Linker Systems: Structural Diversities towards Functional Materials. *CrystEngComm* **2013**, *15*, 9276–9295. [[CrossRef](#)]
41. Bunck, D.N.; Dichtel, W.R. Mixed Linker Strategies for Organic Framework Functionalization. *Chem. A Eur. J.* **2013**, *19*, 818–827. [[CrossRef](#)]
42. Qin, J.S.; Yuan, S.; Wang, Q.; Alsalme, A.; Zhou, H.C. Mixed-Linker Strategy for the Construction of Multifunctional Metal-Organic Frameworks. *J. Mater. Chem. A* **2017**, *5*, 4280–4291. [[CrossRef](#)]
43. Chun, H.; Dybtsev, D.N.; Kim, H.; Kim, K. Synthesis, X-ray Crystal Structures, and Gas Sorption Properties of Pillared Square Grid Nets Based on Paddle-Wheel Motifs: Implications for Hydrogen Storage in Porous Materials. *Chem. A Eur. J.* **2005**, *11*, 3521–3529. [[CrossRef](#)] [[PubMed](#)]
44. Chelucci, G.; Thummel, R.P. Chiral 2,2'-Bipyridines, 1,10-Phenanthrolines, and 2,2':6',2''-Terpyridines: Syntheses and Applications in Asymmetric Homogeneous Catalysis. *Chem. Rev.* **2002**, *102*, 3129–3170. [[CrossRef](#)] [[PubMed](#)]
45. Tu, T.N.; Nguyen, M.V.; Nguyen, H.L.; Yuliarto, B.; Cordova, K.E.; Demir, S. Designing Bipyridine-Functionalized Zirconium Metal-Organic Frameworks as a Platform for Clean Energy and Other Emerging Applications. *Coord. Chem. Rev.* **2018**, *364*, 33–50. [[CrossRef](#)]
46. Manna, K.; Zhang, T.; Greene, F.X.; Lin, W. Bipyridine- and Phenanthroline-Based Metal-Organic Frameworks for Highly Efficient and Tandem Catalytic Organic Transformations via Directed C-H Activation. *J. Am. Chem. Soc.* **2015**, *137*, 2665–2673. [[CrossRef](#)]
47. Manna, K.; Zhang, T.; Lin, W. Postsynthetic Metalation of Bipyridyl-Containing Metal-Organic Frameworks for Highly Efficient Catalytic Organic Transformations. *J. Am. Chem. Soc.* **2014**, *136*, 6566–6569. [[CrossRef](#)]
48. Kent, C.A.; Mehl, B.P.; Ma, L.; Papanikolas, J.M.; Meyer, T.J.; Lin, W. Energy Transfer Dynamics in Metal-Organic Frameworks. *J. Am. Chem. Soc.* **2010**, *132*, 12767–12769. [[CrossRef](#)]
49. Wang, C.; Xie, Z.; deKrafft, K.E.; Lin, W. Doping Metal-Organic Frameworks for Water Oxidation, Carbon Dioxide Reduction, and Organic Photocatalysis. *J. Am. Chem. Soc.* **2011**, *133*, 13445–13454. [[CrossRef](#)]
50. Maza, W.A.; Ahrenholtz, S.R.; Epley, C.C.; Day, C.S.; Morris, A.J. Solvothermal Growth and Photophysical Characterization of a Ruthenium(II) Tris(2,2'-Bipyridine)-Doped Zirconium UiO-67 Metal Organic Framework Thin Film. *J. Phys. Chem. C* **2014**, *118*, 14200–14210. [[CrossRef](#)]

51. Dong, H.; Zhang, X.; Lu, Y.; Yang, Y.; Zhang, Y.P.; Tang, H.L.; Zhang, F.M.; Yang, Z.D.; Sun, X.; Feng, Y. Regulation of Metal Ions in Smart Metal-Cluster Nodes of Metal-Organic Frameworks with Open Metal Sites for Improved Photocatalytic CO₂ Reduction Reaction. *Appl. Catal. B Environ.* **2020**, *276*, 119173. [[CrossRef](#)]
52. Thulasi Karunakaran, S.; Pavithran, R.; Sajeev, M.; Mohan Mohan Rema, S. Photocatalytic Degradation of Methylene Blue Using a Manganese Based Metal Organic Framework. *Results Chem.* **2022**, *4*, 100504. [[CrossRef](#)]
53. Luo, M.; Wang, Y.; Huang, T.; Su, T.; Fu, D.; Yue, S.; Zeng, H. Application of an Mn-MOF as a Highly Efficient Catalyst for Sunlight-Driven Hydrogen Generation. *Phase Transitions* **2018**, *91*, 1179–1187. [[CrossRef](#)]
54. Lu, X.M.; Li, P.Z.; Wang, X.T.; Gao, S.; Wang, X.J.; Wang, S.; Deng, Y.H.; Zhang, Y.J.; Zhou, L. Syntheses, Crystal Structures and Magnetic Behaviors of Three MnII-Terephthalate Coordination Polymers Containing Terminal Ligands. *Polyhedron* **2008**, *27*, 2402–2408. [[CrossRef](#)]
55. Ladrak, T.; Smulders, S.; Roubeau, O.; Teat, S.J.; Gamez, P.; Reedijk, J. Manganese-Based Metal-Organic Frameworks as Heterogeneous Catalysts for the Cyanosilylation of Acetaldehyde. *Eur. J. Inorg. Chem.* **2010**, *24*, 3804–3812. [[CrossRef](#)]
56. Chen, C.X.; Wei, Z.W.; Fan, Y.N.; Su, P.Y.; Ai, Y.Y.; Qiu, Q.F.; Wu, K.; Yin, S.Y.; Pan, M.; Su, C.Y. Visualization of Anisotropic and Stepwise Piezofluorochromism in an MOF Single Crystal. *Chem* **2018**, *4*, 2658–2669. [[CrossRef](#)]
57. Jiang, Y.; Cao, L.; Hu, X.; Ren, Z.; Zhang, C.; Wang, C. Simulating Powder X-ray Diffraction Patterns of Two-Dimensional Materials. *Inorg. Chem.* **2018**, *57*, 15123–15132. [[CrossRef](#)]
58. Leszczyński, M.K.; Justyniak, I.; Gontarczyk, K.; Lewiński, J. Solvent Templating and Structural Dynamics of Fluorinated 2D Cu-Carboxylate MOFs Derived from the Diffusion-Controlled Process. *Inorg. Chem.* **2020**, *59*, 4389–4396. [[CrossRef](#)]
59. Guillermin, V.; Weseliński, Ł.J.; Belmabkhout, Y.; Cairns, A.J.; D’Elia, V.; Wojtas, Ł.; Adil, K.; Eddaoudi, M. Discovery and Introduction of a (3,18)-Connected Net as an Ideal Blueprint for the Design of Metal-Organic Frameworks. *Nat. Chem.* **2014**, *6*, 673–680. [[CrossRef](#)]
60. Vitillo, J.G.; Presti, D.; Luz, I.; Llabrés i Xamena, F.X.; Bordiga, S. Visible-Light-Driven Photocatalytic Coupling of Benzylamine over Titanium-Based MIL-125-NH₂ Metal-Organic Framework: A Mechanistic Study. *J. Phys. Chem. C* **2020**, *124*, 23707–23715. [[CrossRef](#)]
61. Sun, D.; Ye, L.; Li, Z. Visible-Light-Assisted Aerobic Photocatalytic Oxidation of Amines to Imines over NH₂-MIL-125(Ti). *Appl. Catal. B Environ.* **2015**, *164*, 428. [[CrossRef](#)]
62. Yang, X.; Huang, T.; Gao, S.; Cao, R. Boosting Photocatalytic Oxidative Coupling of Amines by a Ru-Complex-Sensitized Metal-Organic Framework. *J. Catal.* **2019**, *378*, 248–255. [[CrossRef](#)]
63. Li, J.; Chang, B.; Zhao, H.; Meng, Q.; Li, M.; Han, Q. Visible-Light-Responsive Polyoxometalate-Based Metal-Organic Framework for Highly Efficient Photocatalytic Oxidative Coupling of Amines. *J. Mater. Sci.* **2021**, *56*, 6676–6688. [[CrossRef](#)]
64. Su, F.; Mathew, S.C.; Möhlmann, L.; Antonietti, M.; Wang, X.; Blechert, S. Aerobic Oxidative Coupling of Amines by Carbon Nitride Photocatalysis with Visible Light. *Angew. Chem. Int. Ed.* **2011**, *50*, 657–660. [[CrossRef](#)] [[PubMed](#)]

Disclaimer/Publisher’s Note: The statements, opinions and data contained in all publications are solely those of the individual author(s) and contributor(s) and not of MDPI and/or the editor(s). MDPI and/or the editor(s) disclaim responsibility for any injury to people or property resulting from any ideas, methods, instructions or products referred to in the content.